NDT&E International 87 (2017) 44–49

Contents lists available at ScienceDirect

NDT&E International

journal homepage: www.elsevier.com/locate/ndteint

Evaluation of mechanical performance of NiCo nanocoated aerospace aluminum alloy using quantitative photo-thermo-mechanical radiometry as a non-contact strain gauge

Huiting Huan[a,b], Andreas Mandelis[a,b,*], Lixian Liu[a,b], Alexander Melnikov[b]

[a] School of Optoelectronic Information, University of Electronic Science and Technology of China, Chengdu 610054, China
[b] Center for Advanced Diffusion-Wave and Photoacoustic Technologies (CADIPT), Department of Mechanical and Industrial Engineering, University of Toronto, Toronto, ON, Canada M5S 3G8

ARTICLE INFO

Keywords:
Thermal diffusivity
Nickel-cobalt (NiCo)
Nanocoating
Non-contact
Non-destructive
Photo-thermo-mechanical radiometry (PTMR)

ABSTRACT

Non-contact photo-thermo-mechanical radiometry (PTMR) was introduced to evaluate the mechanical properties of an aerospace aluminum alloy with Nickel Cobalt (NiCo) coatings. A home-made small-scale tensile rig was used to apply static uniaxial tensile load on the samples. The strength of nanocoated samples was recorded in terms of strain by an adhesive strain gauge also acting as a PTMR calibration device. For the purpose of non-destructive evaluation, the tests were limited within the elastic regime. Two experimental modalities were used: frequency scan at fixed load and strain scan at fixed frequency. The test results were analyzed with both a three-layer and a more detailed five-layer thermo-mechanical-wave (TMW) model. Both theoretical and experimental results indicated that the presence of the NiCo nanocoating can significantly strengthen the mechanical properties of the coated aluminum substrate. The coating can also provide protection to defective substrates and enhance their mechanical stiffness (strength).

1. Introduction

The mechanical performance of aerospace materials in terms of stability and durability is a very important issue in the aerospace industry. To assess and maintain safe and reliable functionality, non-destructive testing (NDT) techniques are widely applied to inspect hidden fatigue and cracks inside aerospace components. Conventional approaches include ultrasound [1,2], spectroscopy [3], X-ray diffraction [4] etc. Invariably these methods are either indirect, requiring complicated instrumentation, or rely on direct contact. In the past decades, several NDT non-contacting methods arose based on the advent of laser sources. Laser ultrasound using modulated laser light to generate thermoelastic waves in the time-domain [5,6] or the frequency-domain [7,8] is such an advanced non-contacting approach for mechanical property evaluation. Despite its wide popularity and non-contact nature, this technique is handicapped due to the severe acoustic impedance mismatch between sample and air, thereby requiring a coupling fluid medium and/or contacting device for modulated laser applications in the frequency-domain, and/or an alternative complex optic detection system (e.g. interferometer) for pulsed laser applications in the time-domain. Moreover, it involves both thermal and acoustic wavefields for signal interpretation which further complicates the problem [9]. Photo-thermal radiometry (PTR) focuses only on the temperature field which is quantitatively determined by the sample thermophysical properties, therefore, it can greatly simplify the NDT process and provide a truly non-contact alternative [10,11]. However, until recently, the PTR link to mechanical properties has been tenuous and quasi-empirical [12].

The connection between thermophysical properties and the mechanical state of a material was theoretically briefly discussed in the classic treatise by Landau and Lifshitz [13] and speculatively by Wong et al. [14]. Possibilities for quantifying the stress-dependence of thermophysical properties were also reported [15,16]. Several authors showed that the thermal conductivity is linearly dependent on the applied external stress within the sample's elastic regime, which is consistent with thermodynamic theory [17–19]. Very recently Huan et al. [19] introduced a quantitative thermo-mechanical-wave (TMW) theoretical framework linking photothermal signals to mechanical strain imposed by an external stress and demonstrated a direct correspondence of the resulting photo-thermo-mechanical radiometry (PTMR) signals to the well-known conventional stress-strain relation across the entire strain axis from the free (unstressed) state to fracture

* Corresponding author at: Center for Advanced Diffusion-Wave and Photoacoustic Technologies, Department of Mechanical and Industrial Engineering, University of Toronto, ON, Canada M5S 3G8.
E-mail address: mandelis@mie.utoronto.ca (A. Mandelis).

http://dx.doi.org/10.1016/j.ndteint.2017.01.004
Received 28 July 2016; Received in revised form 27 December 2016; Accepted 3 January 2017
Available online 10 January 2017
0963-8695/

[19]. In summary, PTMR was shown to act as a non-contact all optical (photothermal) dynamic strain gauge capable of measuring the widest strain range to-date, well beyond the range covered by today's adhesive static strain gauge technologies. Based on these results, the mechanical performance enhancement of nanocoated aerospace substrates was studied in this work using non-contact PTMR.

2. Materials and experimental

The tested samples were made from aerospace aluminum 6061 alloy and machined into a T-shape ("dog-bone") with 2 mm thickness at the probed locations. The samples were then coated with 127 μm (actual thickness) of NiCo nanocoating. These nanocoatings are light-weight hybrid components which combine thin nanostructured metal claddings with polymeric substrates produced by either injection molding or by additive manufacturing methodologies. These nanometal-polymer hybrids provide unique, yet not well understood, combinations of structural, mechanical and functional properties, not achievable in monolithic components. They feature ultrafine grain sizes in nanocrystalline electrodeposits which give yield strengths that can exceed 1250 MPa, while still exhibiting more than 5% uniform plastic strain. For comparison, a horizontal side hole was drilled into one of the aluminum substrates at the waist center, thereby compromising the mechanical strength of the sample before the coating process, as shown in Fig. 1. The coating is used to protect the aluminum substrate from erosion and oxides. It is also supposed to provide extra mechanical support and enhance durability. The experiment setup was the same as in our earlier studies [19] and is shown in Fig. 2. Briefly, a 4-W modulated 808-nm laser with a multimode optical fiber was used as a modulated heat source. A small-scale tensile rig was used to apply axial tensile loading on the samples and a standard aligned PTR optical system was used to detect the laser induced infrared photon emission. To improve the PTMR signal, a washable black paint layer was applied at the waist of the T-shaped samples where most tensile stress concentrates. The experiments included both frequency scan sat various mechanical loads (stresses) and stress-strain scans at a fixed frequency. The PTMR signals were used to determine the extent of the elastic regime and all subsequent experiments were limited within it to ensure the non-destructive character of the tests.

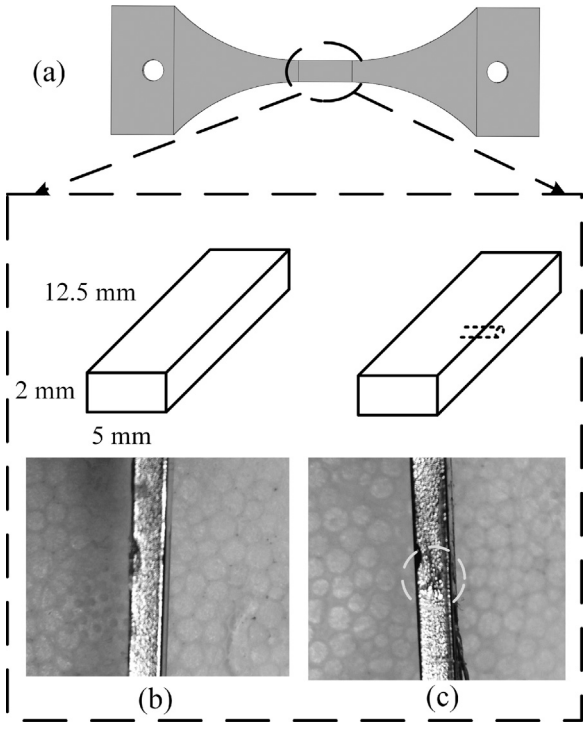

Fig. 1. Tested aerospace sample geometry: (a) 127 μm NiCo nanocoated T-shaped ("dog-bone") sample with aluminum alloy substrate; (b) shape of waist region (center) of the intact coated sample (labelled Sample 1); (c) waist region center of a defective substrate sample with a drilled hole from the side at the center ~1 mm in depth and 1 mm in diameter (labelled Sample 2).

3. Theoretical analysis

PTR has been used for the determination of thermophysical parameters in both single-layer and multi-layer materials with quantitative thermal-wave theory [20]. However, most researchers targeted homogenous and isotropic solids the thermal conductivities of which are constant and uniform. Furthermore, the connection to mechanical properties was not made. In this investigation, the T-shaped alloy nanocoated samples are subjected to uniaxial tensile loading, and as a result, the thermal conductivities of both coating and substrate become anisotropic and functions of mechanical properties [19]. The thermal diffusion equations are generalized to accommodate the tensorial character of the conductivities in the coating and substrate:

$$\rho_1 C_1 \frac{\partial T_1}{\partial t} - \nabla\cdot(\mathbf{k}_1\cdot\nabla T_1) = g \tag{1a}$$

$$\rho_2 C_2 \frac{\partial T_2}{\partial t} - \nabla\cdot(\mathbf{k}_2\cdot\nabla T_2) = 0 \tag{1b}$$

The subscripts 1 and 2 refer to coating and substrate properties, respectively; ρ, C denote the density and specific heat capacity of the two materials, respectively; g is the heat source and $\mathbf{k} = k_{ij}(\boldsymbol{\tau})$, $i, j = x_1, x_2, x_3$ is the stress ($\boldsymbol{\tau}$) dependent thermal conductivity tensor which is symmetric, i.e. $k_{ij} = k_{ji}$. Eqs. 1(a) and 1(b) need to be simplified for analytical solutions. To avoid the complexity of non-isotropic Cartesian coordinates with a directional tensile load and an azimuthally symmetric Gaussian laser beam, the beam was expanded (~8 mm in diameter) so as to reduce the problem of Eqs. (1) to one dimension (depth) and thus simplify the solutions. The one-dimensional (1D) thermo-mechanical-wave equations that incorporate the stress dependent thermal conductivity can be expressed in the frequency domain as follows [19]:

$$\rho_1 C_1 i\omega T_1 - (1+\varepsilon)^2 k_1(\tau_1)\frac{d^2 T_1}{dz^2} = \beta I_0 \delta(z) \tag{2a}$$

$$\rho_2 C_2 i\omega T_2 - (1+\varepsilon)^2 k_2(\tau_2)\frac{d^2 T_2}{dz^2} = 0 \tag{2b}$$

Here ω is the modulation angular frequency $\omega = 2\pi f$, β is the optical-to-thermal energy conversion efficiency, I_0 is the laser intensity and $\delta(z)$ is the Dirac delta function which indicates surface-absorption of the laser beam. As the nanocoating and the substrate are regarded as elastically parallel when subjected to tensile loading, ε is their common strain; τ_1, τ_2 are strain-associated stresses inside the coating and substrate, respectively. Eqs. (2) are similar to conventional thermal-wave equations only with modified thermal conductivity and explicit dependence on strain.

3.1. One-solid-layer model (air-sample-air system)

Although it is strictly improper to lump the three-layer solid structure into one and use a 3-layer model to identify the thermal properties of the coated samples, this theoretical model is approximately valid at low frequencies when the thickness of the coating is small compared to the averaged thermal diffusion length in the solid layered structure. The simplified model can provide effective parameters of the sample which are easy to quantify and analyze. In this approximation, the coupled Eqs. (2) collapse into one equation as the coated sample can be regarded as a single layer with an effective diffusivity α_n surrounded by air of diffusivity α_{am}:

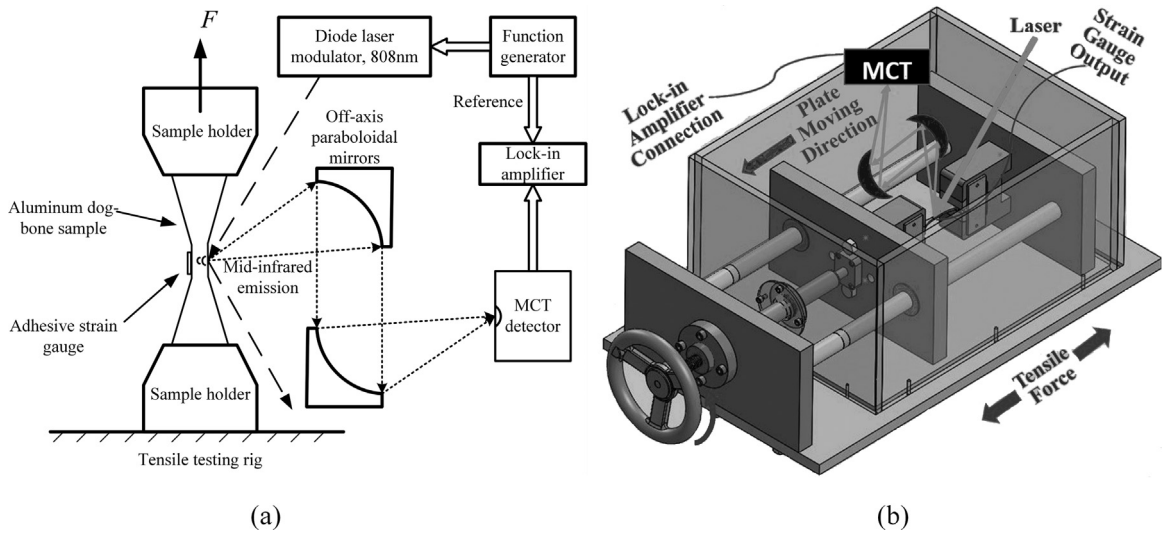

Fig. 2. Schematic diagram of experimental setup: (a) PTMR system accessory of tensile rig which can apply a stress (force) F on a sample; (b) Tensile rig with PTMR accessory. The 808 nm modulated expanded laser beam is incident on a "dog-bone" sample waist. The generated IR emission is collected by a MCT detector and demodulated by a software or hardware lock-in amplifier. The lock-in signal (expressed as amplitude and phase) at various modulation

$$\sigma_n(\tau)T - \frac{d^2T}{dz^2} = \frac{\beta I_0 \delta(z)}{k_n},\ L \le z \le 0 \tag{3a}$$

$$\sigma_{am}T - \frac{d^2T}{dz^2} = 0,\ z \le 0,\ z \ge L \tag{3b}$$

$$\sigma_{am} = \sqrt{i\omega/\alpha_{am}},\ \sigma_n(\tau) = \sqrt{i\omega/\alpha_n(\tau)},\ \alpha_{am} = (k/\rho C)_{am},\ \alpha_n = k_n(\tau)/\rho_n C_n \tag{3c}$$

L is the total thickness of the coated sample, $\sigma_n(\tau)$Z is the thermo-mechanical wavevector in the solid, and σ_{am} is the thermal wavevector in the ambient. The subscript n indicates an effective parameter of the solid layered structure. Due to the fact that air is a very poor heat conductor, the metal-air interface can be regarded as adiabatic with zero-flux [10]. The solution of Eq. 3(a) can be derived in terms of amplitude and phase as functions of frequency:

$$A(f) = \left(\frac{I_0(f)}{e_n\sqrt{f}}\right)\frac{[(1-e^{-2\gamma})^2 + 4e^{-2\gamma}\sin^2\gamma]^{1/2}}{(1-e^{-\gamma}\cos\gamma)^2 + e^{-2\gamma}\sin^2\gamma} \tag{4a}$$

$$\Phi(f) = \arctan\left(\frac{-2e^{-\gamma}\sin\gamma}{1-e^{-2\gamma}}\right) - \frac{\pi}{4} \tag{4b}$$

where $e_n(\tau) = \sqrt{k_n(\tau)\rho_n C_n}$ is the effective thermal effusivity of the sample, and $\gamma \equiv 2\sqrt{\pi f}\kappa_n(\tau)$ and $\kappa_n(\tau) \equiv L/\sqrt{\alpha_n(\tau)}$ are thermophysical and dimensional parameter groupings naturally occurring in the solution of the equation. Instead of quantifying stress-dependent thermal parameters for each layer, Eqs. (4) ignore the difference between coating and substrate and regard them as one object, thus simplifying computation. It can be noted that phase is only related to parameter γ and is independent of laser parameters, which renders it simpler and more useful than amplitude [19].

3.2. Three-solid-layer model (air-coating-aluminum-coating-air system)

The effective parameters derived through the three-layer TMW model are unable to separate out the individual contributions from coating and substrate. Given that the NiCo nanocoating has very different (not well known) thermophysical properties from the aluminum substrate, a five-layer model was established to determine the properties of coating and substrate separately.

The five-layer model is shown in Fig. 3. Using the nanocoating surface absorption assumption, the equations for the five layers are:

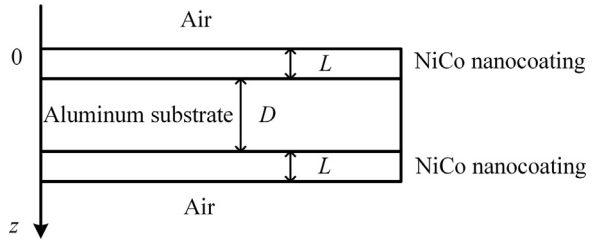

Fig. 3. Schematic of five-layer TMW model.

$$\sigma_c T_{1c} - d^2T_{1c}/dz^2 = \beta I_0 \delta(z)/k_1,\ L \le z \le 0 \tag{5a}$$

$$\sigma_s T_s - d^2T_s/dz^2 = 0,\ L \le z \le D + L \tag{5b}$$

$$\sigma_c T_{2c} - d^2T_{2c}/dz^2 = 0,\ D + L \le z \le D + 2L \tag{5c}$$

$$\sigma_{am} T_{am} - d^2T_{am}/dz^2 = 0,\ z \le 0,\ z \ge D + 2L \tag{5d}$$

The subscripts c and s represent parameters of coating and substrate, respectively and they both are stress dependent. Solutions to Eqs. (5) for the five layers can be written as follows:

$$T_{am}(z,\omega) = C_1 e^{\sigma_{am} z},\ z \le 0 \tag{6a}$$

$$T_{1c}(z,\omega) = A_1 e^{-\sigma_c z} + A_2 e^{\sigma_c z},\ 0 \le z \le L \tag{6b}$$

$$T_s(z,\omega) = B_1 e^{-\sigma_s(z-L)} + B_2 e^{\sigma_s(z-L)},\ L \le z \le L + D \tag{6c}$$

$$T_{2c}(z,\omega) = A_3 e^{-\sigma_c(z-L-D)} + A_4 e^{\sigma_c(z-L-D)},\ L + D \le z \le 2L + D \tag{6d}$$

$$T_{am}(z,\omega) = C_2 e^{-\sigma_{am}(z-2L-D)},\ z \ge 2L + D \tag{6e}$$

It is assumed that the temperature and heat flux at the boundaries between layers are continuous. Solving for the coating temperature distribution at the front surface (z=0) from which the infrared emission is collected:

$$T_1(0,\omega) = C_1 = \frac{\beta I[\rho_{120}e^{2\sigma_2 D} - \gamma_{12} + (1-\rho_{120}\gamma_{12}e^{2\sigma_2 D})e^{-2\sigma_1 L}]}{k_1\sigma_1(1+b_{01})(\gamma_{12}+\gamma_{01}e^{-2\sigma_1 L})(\rho_{120}^2 e^{2\sigma_2 D} - 1)}$$

$$\rho_{120} = \frac{1+\gamma_{12}\gamma_{01}e^{-2\sigma_1 L}}{\gamma_{12}+\gamma_{01}e^{-2\sigma_1 L}},\ \gamma_{ij} = \frac{1-b_{ij}}{1+b_{ij}},\ b_{ij} = \frac{e_i}{e_j} = \frac{k_i\sigma_i}{k_j\sigma_j} \tag{7}$$

e_i is the effusivity of layer i, and γ_{ij} is the thermal coupling coefficient between layer i and j. Eq. (7) involves separate parameters of coating and substrate and thus yields a higher resolution solution than the

three-layer model. Some assumptions can be made for simplicity: Within the elastic regime, i) the thermal conductivities (and thus also the thermal diffusivities) of both coating and substrate are the only strain dependent thermophysical properties; ii) the functional connection between thermal conductivity and strain is linear:

$$k_1 = k_1^0 + R_1 \cdot \varepsilon$$
$$\alpha_1 = \alpha_1^0 + Q_1 \cdot \varepsilon \quad (8a)$$

$$k_2 = k_2^0 + R_2 \cdot \varepsilon$$
$$\alpha_2 = \alpha_2^0 + Q_2 \cdot \varepsilon \quad (8b)$$

The superscript 0 indicates the parameters at zero-stress, $R_1 = dk_1/d\varepsilon = Q_1\rho_1C_1$, $R_2 = dk_2/d\varepsilon = Q_2\rho_2C_2$ are proportionality factors. As the properties of different materials can vary over large ranges, and they can also be method and test dependent, average parameters were taken for the NiCo nanocrystalline coating and aluminum substrate (k_1^0=154.8 W/m K, α_1^0=6.4×10^{-5} m^2/s, k_2^0=90 W/m K, α_2^0=2.35×10^{-5} m^2/s) [21,22].

4. Results and discussion

4.1. Frequency scan (FS) and stress scan (SS) results

The frequency range was kept low (scanned from 0.5 to 16 Hz) to ensure the TMW diffusion length was long enough to cover the entire thickness of the samples. At each frequency, the signal data were averaged 40 times within 3 min. The recorded phase signals were normalized to the zero-stress data and plotted in the form of phase differences. For the *coated intact sample* (labelled Sample 1) and *coated defective substrate sample* (labelled Sample 2), within the elastic regime the phase differences at four different states of stress are shown in Fig. 4(a). Specifically, Fig. 4(b) shows the FS results from samples 1, 2 and a reference sample (bare aluminum substrate) at similar stress levels. The figures qualitatively indicate that sample 1 exhibits the best mechanical performance among all three samples as the stress associated signal undergoes the least change. Additionally, without the protection of a coating, the bare aluminum sample shows the largest stress dependent signal change.

High-stress-resolution SS phase difference data at fixed frequencies are shown in Fig. 5. The samples were subjected to several of loading and reversed (unloading) cycles. The signal data were averaged 20 times within 90 s at each strain level. All results from the three samples have high signal-to-noise ratio (SNR) and show good reproducibility and reversibility within the elastic regime. Consistently with the FS results, sample 1 shows the best stability with the least phase changes (only up to 0.5°).

4.2. Quantitative analysis

Both the FS and SS results can be best-fitted to Eqs. (4) to quantify the thermal diffusivity and effusivity of the tested samples. In this work

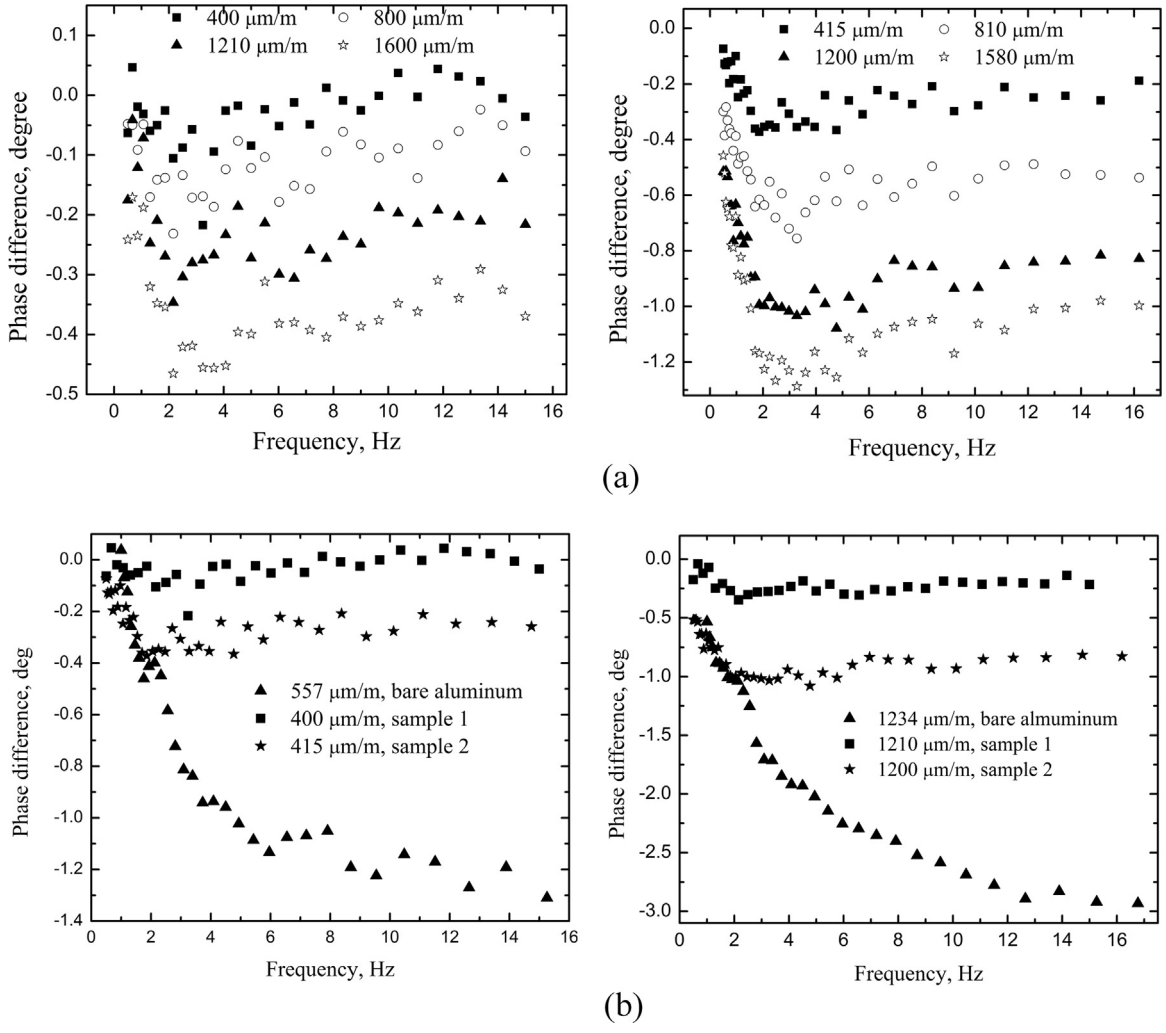

Fig. 4. : Phase differences refer to zero-stress; (a) intact coated sample (sample 1, left) and defective substrate coated sample (sample 2, right); (b) three groups of sample under medium stress (left) and high stress (right).

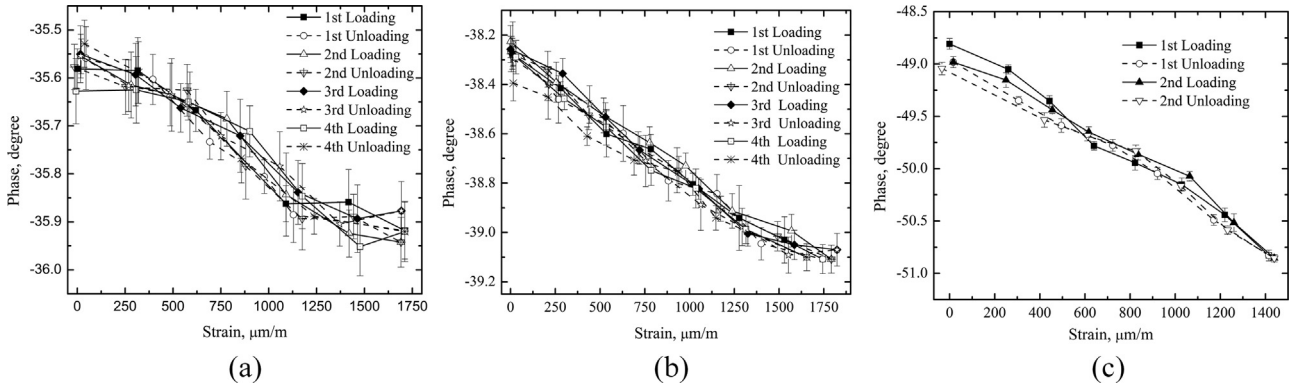

Fig. 5. : Phase signals vs strain from stress scans at fixed frequencies within the elastic regime; (a) intact coated Sample 1 (f =2.03 Hz); (b) defective coated substrate Sample 2 (f =1.07 Hz); (c) bare aluminum substrate reference sample (f =2.5 Hz, redrawn from Ref. [19]).

only the phase channels of the PTMR signals were used for data analysis as they showed better stability and reproducibility than amplitudes, in agreement with our previous studies [19]. Since phase is independent of effusivity, Eq. (4b), this parameter will not be considered henceforth. To minimize the inaccuracy impact of multi-layers in samples 1 and 2 to the simplified model, it was necessary to choose only the lowest frequency range (0.5–5 Hz) for data fitting. The results are shown in Fig. 6(a). Both FS- and SS-derived parameters indicate linear strain dependencies of the (effective) thermal diffusivities of all three samples in excellent agreement between the two measurement methods for the reference sample and sample 1. The larger discrepancy between FS and SS with respect to sample 2 is understood due to the defect in the substrate. The strain values on the x-axis were independently obtained from the attached strain gauges over the entire elastic regime. These curves can be used as calibration data for making PTMR a quantitative strain gauge methodology.

A higher resolution analysis for the coated samples was subsequently performed by fitting the FS and SS phase data to Eq. (7) using Eqs. (8). The full frequency range (0.5 Hz~16 Hz) data were used for fitting. The thermal diffusivities of coating and substrate were extracted

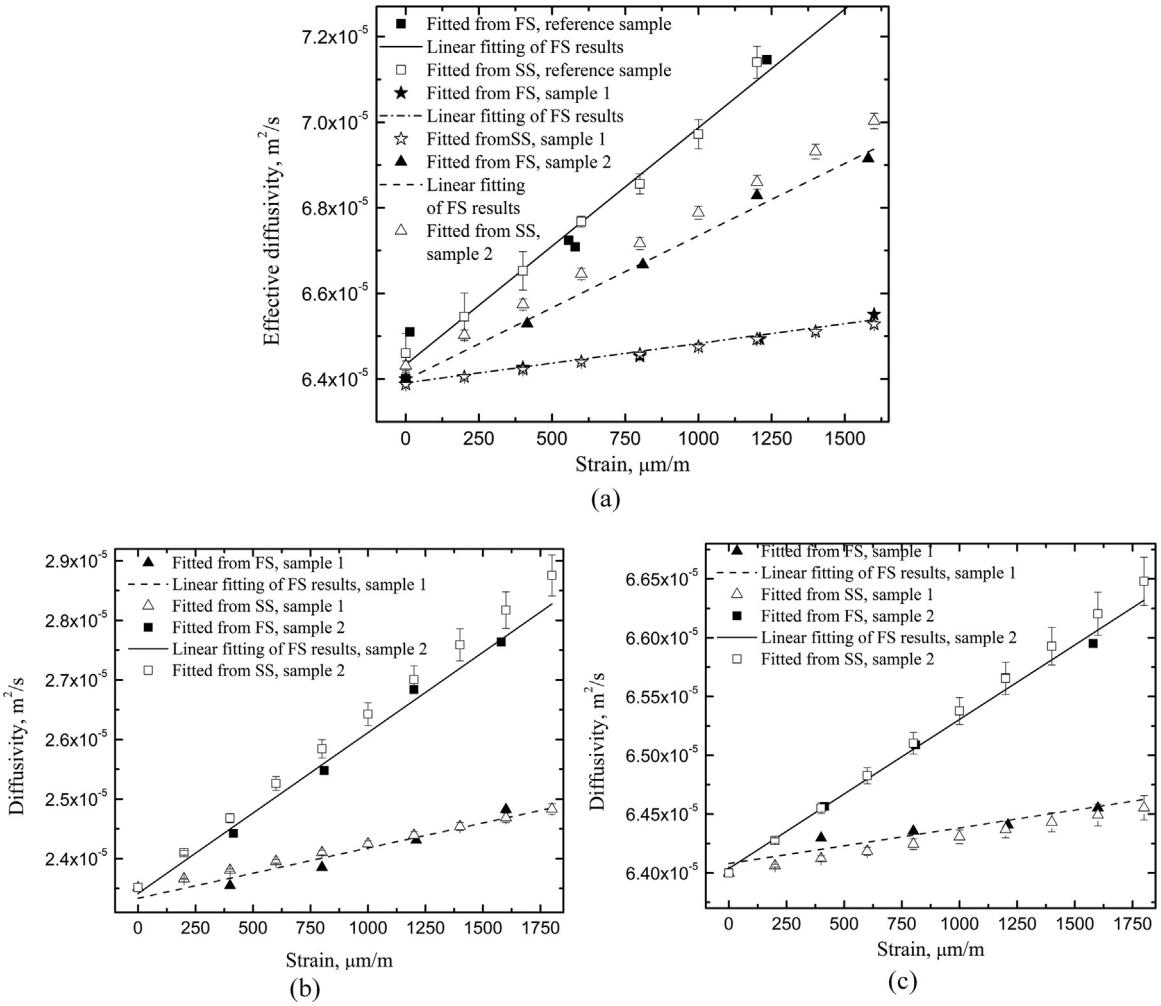

Fig. 6. Thermal diffusivity strain dependencies quantified from frequency scan (FS) and stress scan (SS) data. (a) Effective thermal diffusivity fitted to Eqs. (4) for the three samples (reference sample results were redrawn from [19]); (b) Thermal diffusivity of NiCo coating and (c) of aluminum substrate fitted to Eq. (7) using Eqs. (8).

Table 1.
The relative change of thermal diffusivity of the samples at 1200 μm/m strain.

Sample	(Effective) diffusivity change	Diffusivity change of the NiCo coating	Diffusivity change of the aluminum substrate	Proportionality factor Q of the NiCo coating (m^2/s)	Proportionality factor Q of the aluminum substrate (m^2/s)
Reference sample	11%	–	–	–	5.5×10^{-3}
Sample 1	1.6%	3.4%	0.55%	7.3×10^{-4}	3.1×10^{-4}
Sample 2	6.1%	17%	2.3% (effective)	2.9×10^{-3}	1.4×10^{-3} (effective)

independently, as depicted in Fig. 6(b) and (c). These results also exhibit linear relations in both coating and substrate for the both samples. The FS and SS determined thermal diffusivities show excellent consistency.

Table 1 shows the thermal diffusivity changes obtained using the two theoretical models for all samples at fixed strain. The diffusivity-strain proportional factors of both coating and aluminum substrate were also calculated from the three-solid-layer model for sample 1 and sample 2, one-solid-layer model for the reference sample. For the defective aluminum substrate, the stretch is larger for both substrate and coating at the same strain (obtained under different stress), thus the coating undergoes more deformation and therefore larger thermal diffusivity change. At the same strain, the defective substrate sample undergoes larger tensile loading because its waist is more “yielding” (less resistive to external stress) than the intact substrate. Therefore, it elongates more and so does the coating. The results demonstrate that NiCo nanocoating can substantially enhance the mechanical performance of the aluminum substrate by acting as a protective elastic layer, in addition to its general anti-corrosion and anti-abrasion capabilities. The nanocoating layer over the defective substrate aluminum also provides outstanding mechanical stiffness which far outperforms the mechanical strength of the bare aluminum reference within the elastic regime.

5. Conclusions

As a fully non-destructive and non-contacting methodology, PTMR was proven to be capable of evaluating the mechanical strength of nanocoated materials subjected to external loads by quantifying the applied strain based on derivations of thermophysical property (thermal conductivity, effusivity, and diffusivity) dependence on strain. In conjunction with a multilayer thermo-mechanical-wave model, PTMR quantitatively determined changes in the stress dependent diffusivity of each layer at fixed strain, thereby measuring the stiffness (mechanical strength or resistance to external force) of the layer. A simplified one-solid-layer model was also able to yield consistent effective stiffness trends through thickness-averaged diffusivity changes at fixed strain (but without layer-by-layer resolution). The measurements of the conductivity and diffusivity vs. strain coefficients R and Q, respectively, render PTMR into a non-contacting *quantitative* optical (photothermal) strain gauge capable of resolving intralayer strains. The application of PTMR to nanocoated NiCo aerospace aluminum alloy substrates demonstrated the degree of mechanical strength (and protection) afforded coated intact and defective samples, compared to an uncoated reference and can be used for assessing the effectiveness of the coating process toward strengthening the mechanical properties of the substrate.

Acknowledgements

The authors are grateful to the Natural Sciences and Engineering Research Council of Canada (NSERC) for a 2016 Engage Grant to AM with Integran Technologies, Mississauga, ON; for a Discovery grant to AM; and to the Canada Research Chairs program. AM also gratefully acknowledges the Chinese Recruitment Program of Global Experts (Thousand Talents). He also acknowledges the Foundation for Innovative Research Groups of the National Natural Science Foundation of China (Grant No. 61421002). HH gratefully acknowledges the China Scholarship Council (CSC) program (No. 201406070045). The authors are grateful to the University of Toronto 4th year Capstone 2015-16 project team (Q. Cao, F. Chang, L.S. Mu, and L. Tian).

References

[1] Crecraft DI. The measurement of applied and residual stresses in metals using ultrasonic waves. J Sound Vib 1967;5:173–92.
[2] Hsu NN. Acoustical birefringence and the use of ultrasonic waves for experimental stress analysis. Exp Mech 1974;14:169–76.
[3] Gogotsi Y, Baek C, Kirscht F. Raman microspectroscopy study of processing-induced phase transformations and residual stress in silicon. Semicond Sci Technol 1999;14:936–44.
[4] Moore M, Evans W. Mathematical correction for stress in removed layers in X-ray diffraction residual stress analysis. SAE Tech Pap 1958. http://dx.doi.org/10.4271/580035, [No. 580035].
[5] Hutchins DA, Nadeau F, Cielo P. A pulsed photoacoustic investigation of ultrasonic mode conversion. Can J Phys 1986;64:1334–40.
[6] Arnold W, Betz B, Hoffmann B. Efficient generation of surface acoustic waves by thermoelasticity. Appl Phys Lett 1985;47:672–4.
[7] Muratikov KL. Theory of stress influence on the photoacoustic thermoelastic signal near the vertical crack tips. Rev Sci Instr 2003;74:722–4.
[8] Huan H, Mandelis A, Lashkari B, Liu L. Frequency-domain laser ultrasound (FDLU) non-destructive evaluation of stress/strain behavior in an aluminum alloy. Int J Thermophys 2017, [in-press].
[9] Husson D, Kino GS. A perturbation theory for acoustoelastic effects. J Appl Phys 1982;53:7250–8.
[10] Balderas-López JA, Mandelis A. Self-normalized photothermal technique for accurate thermal diffusivity measurements in thick metal layers. Rev Sci Instr 2003;74:5219–25.
[11] Munidasa M, Mandelis A, Ball M. Buried thermoplastic layer diagnostics by the use of combined frequency-domain and impulse response photo-thermo-mechanical radiometry. Rev Sci Instrum 1998;69:507–11.
[12] Garcia JA, Mandelis A, Farahbakhsh B, Lebowitz C, Harris I. Thermophysical properties of thermal sprayed coatings on carbon steel substrates by photothermal radiometry. Int J Thermophys 1999;20:1587–602.
[13] Landau LD, Lifshitz EM. Theory of elasticity, 15–17. Bristol: Pergamon Press; 1959. p. 119–22.
[14] Wong AK, Jones R, Sparrow JG. Thermoelastic constant or thermoelastic parameter?. J Phys Chem Solids 1987;48:749–53.
[15] Wang Y, Wright NT. A relationship between thermal diffusivity and finite deformation of polymers. Int J Thermophys 2005;26:1849–59.
[16] Mzali F, Albouchi F, Nasrallah SB, Petit D. Optimal experiment design and thermo-physical characterization of a plastically deformed solid. Inverse Probl Sci Eng 2009;17:335–45.
[17] Muratikov KL, Glazov AL, Rose DN, Dumar JE. Photoacoustic effect in stressed elastic solids. J Appl Phys 2000;88:2948–55.
[18] Pron H, Bissieux C. 3-D thermal modelling applied to stress-induced anisotropy of thermal conductivity. Int J Therm Sci 2004;43:1161–9.
[19] Huan H, Mandelis A, Liu L, Melnikov A. Non-destructive and non-contacting stress-strain characterization of aerospace metallic alloys using photo-thermal-mechanical radiometry. NDTE Int 2016;84:47–53.
[20] Mandelis A. Diffusion-wave fields: mathematical methods and Green functions. New York: Springer; 2001. p. 2.
[21] Powell RW, Tye RP, Hickman MJ. The thermal conductivity of nickel. Int J Heat Mass Transf 1965;8:679–88.
[22] Cverna F. ASM ready reference - thermal properties of metals. ASM Int 2002, [chap. 3 and 4; online at] ⟨http://app.knovel.com/hotlink/toc/id:kpASMRRTP1/asm-ready-reference-thermal/asm-ready-reference-thermal⟩.